

©2016, Elsevier. Licensed under the Creative Commons Attribution-NonCommercial-NoDerivatives 4.0 International <http://creativecommons.org/about/downloads>



***Adding functionality with additive manufacturing: Fabrication of titanium-based antibiotic eluting implants***

Sophie C. Cox<sup>1</sup>, Parastoo Jamshidi<sup>2</sup>, Neil M. Eisenstein<sup>1</sup>, Mark A. Webber<sup>3</sup>, Hany Hassanin<sup>2</sup>, Moataz Attallah<sup>2</sup>, Duncan E.T. Shepherd<sup>4</sup>, Owen Addison<sup>5</sup>, Liam M. Grover<sup>1</sup>

<sup>1</sup>School of Chemical Engineering, University of Birmingham, Edgbaston, B15 2TT, UK

<sup>2</sup>School of Materials and Metallurgy, University of Birmingham, Edgbaston, B15 2TT, UK

<sup>3</sup>School of Biosciences University of Birmingham, Edgbaston, B15 2TT, UK

<sup>4</sup>Department of Mechanical Engineering, School of Engineering, University of Birmingham, Edgbaston, B15 2TT, UK

<sup>5</sup>School of Dentistry, University of Birmingham, Edgbaston, B15 2TT, UK

## **Abstract**

Additive manufacturing technologies have been utilised in healthcare to create patient-specific implants. This study demonstrates the potential to add new implant functionality by further exploiting the design flexibility of these technologies. Selective laser melting was used to manufacture titanium-based (Ti-6Al-4V) implants containing a reservoir. Pore channels, connecting the implant surface to the reservoir, were incorporated to facilitate antibiotic delivery. An injectable brushite, calciumphosphate cement, was formulated as a carrier vehicle for gentamicin. Incorporation of the antibiotic significantly ( $p=0.01$ ) improved the compressive strength ( $5.8\pm 0.7$  MPa) of the cement compared to non-antibiotic samples. The controlled release of gentamicin sulphate from the calcium phosphate cement injected into the implant reservoir was demonstrated in short term elution studies using ultraviolet visible spectroscopy. Orientation of the implant pore channels were shown, using micro-computed tomography, to impact design reproducibility and the back-pressure generated during cement injection which ultimately altered porosity. The amount of antibiotic released from all implant designs over a 6 hour period (28% of the total amount) were found to exceed the minimum inhibitory concentrations of *Staphylococcus aureus* ( $16\ \mu\text{g/mL}$ ) and *Staphylococcus epidermidis* ( $1\ \mu\text{g/mL}$ ); two bacterial species commonly associated with periprosthetic infections. Antibacterial efficacy was confirmed against both bacterial cultures using an agar diffusion assay. Interestingly, pore channel orientation was shown to influence the directionality of inhibition zones. Promisingly, this work demonstrates the potential to additively manufacture a titanium-based antibiotic eluting implant, which is an attractive alternative to current treatment strategies of periprosthetic infections.

## **1. Introduction**

Generally, total joint arthroplasty is a successful procedure that restores function and improves patient quality of life. Despite the introduction of standardised strategies, such as laminar flow clean air operating rooms and pre-operative antibiotics, periprosthetic infection still occurs in approximately 1–2% of patients following a total joint arthroplasty procedure [1] and [2]. When periprosthetic infections do occur they can lead to a need for rescue or revision surgery, and ultimately device failure. As such, implant infection represents one of the most costly complications in orthopaedic surgery.

Clinical procedures for the treatment of periprosthetic infection, include irrigation and debridement with component retention [3], as well as one- and two-stage exchange arthroplasty [4] and [5]. Two-stage exchange arthroplasty involves the implantation of an interim antibiotic-loaded component after removal of the original components. Commonly, antibiotic-loaded polymethylmethacrylate (PMMA) is used in the form of beads or cast into a mould and implanted [6], [7] and [8]. PMMA cements set via an exothermic reaction, reaching temperatures between 70 and 120 °C [9]. This thermal behaviour limits the antibiotics PMMA may be combined with and it has been shown to result in tissue necrosis [10] and [11]. Other disadvantages include chemical necrosis due to leakage of unreacted monomer, shrinkage during polymerisation, and its inability to be resorbed [12]. The interim period in a two-stage exchange arthroplasty may range from 6 to 12 weeks depending on individual surgeon decision, and evidence of infection clearance and healing [13]. During this time, patients may be encouraged to walk with partial weight-bearing [14]. Complications associated with the interim period include sacral pressure sores and fractures on re-implantation [14]. Furthermore, increased morbidity from two-stage compared to one-stage exchange has been reported [15]. Some of these complications may be associated with the inactivity of the patient between procedures in a two-stage exchange arthroplasty.

Current orthopaedic implants are manufactured from stainless steels, cobalt chromium molybdenum alloys, and titanium alloys using traditional manufacturing methods (e.g. machining, forging, and investment casting) [16]. These processes have been optimised over a number of decades resulting in implants that can withstand long-term cyclic loading. In recent years, the use of additive manufacturing (AM) techniques in medicine has gained much attention [17], [18], [19], [20] and [21]. Generally, AM techniques use a layer-by-layer approach to build parts from computer aided design (CAD) models. In comparison to conventional methods, this approach enables material wastage to be reduced and greater geometrical design freedom.

Selective laser melting (SLM) is an AM technology that may be used to manufacture metal components [22], [23], [24] and [25]. During this process, a focused laser beam is used to selectively heat a bed of metallic powder above the materials melting point causing the particles to melt and fuse together. After completion of

each two-dimensional (2D) layer, the build platform is lowered by a pre-set thickness and the coating blade spreads a fresh layer of powder on top. This process is repeated until the full 3-dimensional (3D) geometry has been built. All processing is conducted in a chamber flooded with inert gas, usually nitrogen or argon to minimise oxygen-content.

To date, bone prostheses manufactured via AM technologies have primarily been employed clinically in relatively low load-bearing areas, such as the Food and Drug Administration approved OsteoFab® (Oxford Performance Materials); a patient specific polymer based cranial device. The introduction of metallic AM implants in high fatigue applications, such as permanent components of hip or knee implants, has been hindered by their rough surface features acting as fatigue crack initiation sites. Shorter fatigue life has been previously demonstrated through a comparative fatigue study of additively manufactured and equivalent rolled Ti-6Al-4V dental implants [26].

In the context of the challenges discussed above, the use of a device that would enable patients to fully weight-bear whilst eluting antibiotics during the interim period of a two-stage exchange arthroplasty is an attractive concept. This could be achieved by manufacturing an implant that is mechanically robust enough to withstand the patient's weight but also contains a reservoir that could be filled with an injectable antibiotic eluting biomaterial. To maintain and tailor structural properties a honeycomb type lattice could be introduced within the reservoir region. The geometrical freedom possible from AM technologies would facilitate the manufacture of such an intricate internal architecture, which would not be possible via traditional methods. Furthermore, if the device was used only in the interim period this would circumvent any long-term fatigue issues. Design of a metallic device that satisfies mechanical criteria would remove this demand from the antibiotic eluting material allowing for selection to be solely focused on desired therapeutic properties. This strategy in comparison to the use of antibiotic-loaded PMMA, which must fulfil both mechanical and therapeutic demands, may present advantages.

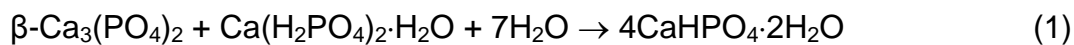
This paper presents a preliminary study to assess the feasibility of utilising SLM to manufacture an antibiotic eluting implant. Simplified cylindrical implants were designed to incorporate a reservoir connected to the surface extremities via a series of channels. A calcium phosphate cement, brushite, was selected as an antibiotic carrier and injected into the AM metallic implant. This material was chosen since, in comparison to PMMA, it sets at lower temperatures and is highly resorbable at physiological conditions [27]. The influence of pore orientation (horizontal, vertical, 45° incline) on the release profile of gentamicin sulphate from the implant was assessed. Antibacterial efficacy was demonstrated against two bacterial species commonly associated with periprosthetic infections. Overall, this work highlights the potential to add further value and functionality to orthopaedic implants by exploiting the advantages that AM technologies bring to manufacturing.

## 2. **Materials and Methods**

### 2.1 *Brushite cement formulation*

Dicalcium phosphate dihydrate (CaHPO<sub>4</sub>·2H<sub>2</sub>O) (DCPD), otherwise known as brushite, is a calcium phosphate phase that is several orders of magnitude more soluble than hydroxyapatite in physiological conditions [27]. Clinically, cements with a high injectability and a setting time between 5 and 15 min are desirable as this allows time for prosthesis implantation and adjustment but does not prolong the operation excessively.

A brushite cement formulation with an injectability of > 80% through a 15G (1.829 mm) needle and a setting time of approximately 12 min was preselected for this study (data not shown). The cement was formulated using β-tricalcium phosphate (β-Ca<sub>3</sub>(PO<sub>4</sub>)<sub>2</sub>) (β-TCP) synthesised using a previously reported method [28]. β-TCP and monocalcium phosphate monohydrate (Ca(H<sub>2</sub>PO<sub>4</sub>)<sub>2</sub>·H<sub>2</sub>O, Innophos, USA) (MCPM) powders were dry mixed in stoichiometric ratios (Eq. (1)) for 30 s using a spatula. The powder components were then mixed with deionised water at a 2:1 powder-to-liquid ratio (PLR) for 30 s to form a workable paste.



Antibiotic loaded brushite cements were prepared by dissolving gentamicin sulphate (Sigma Aldrich, UK) at a concentration of 100 mg/mL into deionised water prior to mixing with the powder components giving a final concentration of 50 mg per 1g of cement.

### 2.2 *Manufacture of cement cylinders*

Prepared cement pastes (Section 2.1) were formed into cylinders (diameter = 6 mm; height = 12 mm) by either casting or injecting into a PTFE split mould. Cast cylinders were made by pouring cement paste into the mould positioned on a Denstar-500 powered vibrating platform (Denstar, Korea). Injected cylinders were formed by loading cement pastes into a 5 mL syringe with 15G (1.829 mm internal diameter) needle after mixing and injecting into the split mould. Both cast and injected cement cylinders were left to set in the mould for 1 h in an incubator at 37 °C, demoulded, and stored in an incubator at 37 °C until use. Injected cement cylinders were manufactured so as to simulate the intended clinical delivery method and this was compared with cast versions (n = 10) as this is the typical process used in the literature [29] and [30].

### 2.3 *Additive manufacture of implant models*

Implant models (Fig. 1a) were fabricated from Ti-6Al-4V gas atomised powder (TLS Technik, Germany) sized 20–50 μm using a M2 Cusing® SLM system (Concept Laser, Germany), which employs an Nd:YAG laser with a wavelength of 1075 nm, spot size of 60 μm and a maximum laser output power of 400 W. The process parameters were optimised to reduce residual porosity and achieve the designed hole geometry for elution of gentamicin. The parameters used were 150 W laser

power, 1750 mm/s scanning speed, 20  $\mu\text{m}$  slice thickness, and hatch spacing of 75  $\mu\text{m}$ . Support structures were built between the substrate base and each individual implant to provide stability during the build. Manufacture was conducted in a chamber flooded with argon gas to minimise oxygen pick-up to  $< 0.1\%$ .

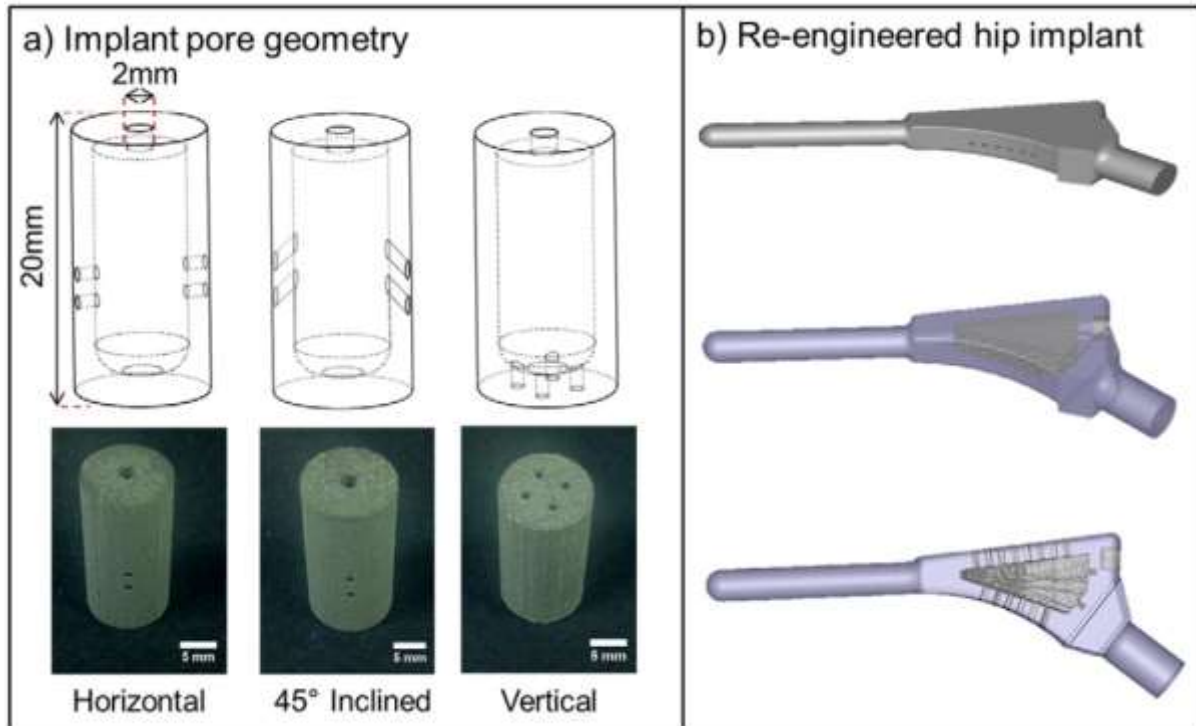


Figure 1: Implant models a) CAD schematics and photomicrographs of Ti-6Al-4V implants manufactured via selective laser melting with 1 mm horizontal, inclined, and vertical pore orientations, and b) re-engineered demonstration hip prostheses of varying transparency designed using Solidworks.

#### 2.4 Loading implants with cement paste

Prepared cement pastes were loaded into 5 mL syringes attached to a 15G needle and injected into the single 2 mm diameter hole at the top of all cylindrical designs (Fig. 1).

#### 2.5 Characterisation of materials

##### 2.5.1 Cement composition

X-ray diffraction (XRD) analysis of set cements was performed on a Bruker D8 Advance Diffractometer (ASX GmbH, Bruker, Germany). Cement cylinders were prepared (Section 2.1) and ground into a fine powder using a pestle and mortar. Approximately 500 mg of the powder was distributed over a 10 mm diameter circular area of Scotch tape (3 M, UK) and attached to the sample holder. Data were collected over a  $2\theta$  range of  $5\text{--}60^\circ$  with a step size of  $0.02^\circ$  and a count time of 0.5 s

per step. Diffraction patterns were matched with the International Centre for Diffraction Data (ICDD) standards using EVA software (version 3.1, Bruker).

### 2.5.2 Cement morphology

Cement segments were attached to aluminium stubs using conducting silver paint and sputter coated with gold in an argon purged chamber for 120 s. Micrographs of cement surfaces were obtained using an EVO MA 10 scanning electron microscope (Carl Zeiss Ltd, UK).

### 2.5.3 Cement compressive strength

Geometrical measurements of nominally identical cement cylinders were taken using digital callipers and the mass of each specimen was measured. Each cylinder was mounted on the lower anvil of a Z030 universal testing machine (Zwick, UK) with its long axis perpendicular to the surface of the anvil. A minimum of 10 samples were compressed to failure at a constant rate of 1 mm/min. The ultimate compressive strength ( $\sigma$ ) was calculated from the maximum load recorded throughout each test (Eq. (2)). Young's modulus ( $E$ ) was determined from the linear region of the stress strain graph using linear regression (Eq. (3)).

$$\sigma = \frac{F}{A} \quad 2$$

$$E = \frac{Fl_0}{A(l-l_0)} = \frac{\sigma}{\varepsilon} \quad 3$$

where  $F$  is force,  $A$  original area,  $l_0$  original length of specimen,  $l$  compressed length of specimen, and  $\varepsilon$  specimen strain.

### 2.5.4 Cement density

The apparent density of cement samples was calculated from geometrical and mass measurements made prior to the mechanical testing. After compression testing, cement fragments were collected and used to determine the true density using a helium pycnometer (Accupyc 1330, Micromeritics, UK). The sample chamber was purged with helium five times before five consecutive measurements of volume were performed. For each sample set, the true density of three different cement cylinders was determined so that reported values were a mean of 15 measurements. Relative porosity was calculated from the values of true and apparent density.

### 2.5.5 Micro-computer tomography

Cement cylinders were scanned using a Skyscan1172 micro-computed tomography (micro-CT) system (Bruker, Belgium) with 80 kV maximum X-ray energy, 8 W beam power, 570 ms exposure per projection, 0.5 mm aluminium filter, and 4.87  $\mu\text{m}$  pixel size. Empty and filled SLM implant models were also scanned with 80 kV maximum X-ray energy, 8 W beam power, 2000 ms exposure per projection, aluminium and copper filter, and 5.95  $\mu\text{m}$  pixel size. Reconstructed data were visualised in 2D and 3D using DataViewer (version 1.5.1.2, Bruker) and CTVOX (version 3.0, Bruker) software, respectively.



A porosity analysis of cast, injected, and injected gentamicin-loaded cement cylinders was conducted using CTAn (version 1.15.4.0, Bruker) software. Briefly, a circle was fitted to the external edges of the cement cylinder to create a region of interest (ROI). This ROI was interpolated across 100 slices positioned in the middle of the longitudinal axis (y-axis) of the sample volume to create a volume of interest (VOI). A global thresholding was applied to create a binary image, which was then filtered to remove noise, and a ROI shrink wrap function used to define the sample extremities. 3D analysis was run over this VOI to determine total, open, and closed porosity as well as the size distribution of open and closed pores. Micro-CT values of porosity were compared with those obtained from true density measurements.  $\beta$ -TCP content of the cement VOI was calculated by conducting 3D analysis of greyscale values defined as unreacted phase and compared with the total solid volume calculated for the same VOI.

To validate CAD implant model geometries, measurements of the pores were obtained from binary micro-CT slice data and compared with designed dimensions (1000  $\mu\text{m}$ ). Four measurements of each pore were taken so that mean values for each design were calculated from a total of 16 measurements.

#### *2.5.6 Release of gentamicin*

Gentamicin release studies were conducted by immersing cement cylinders and implant models containing injected cement in 10 mL of phosphate buffered saline (PBS) stirred at 100 rpm and incubated at 37 °C. Every 30 min up to 3 h and every hour from 3 to 6 h, 10 mL was withdrawn from each sample ( $n = 3$ ) and assayed for gentamicin by measuring the absorbance at 246 nm using a CE 7500 UV–Vis spectrophotometer (Cecil Instruments, UK). Samples of cement without gentamicin were also assayed and the blank subtracted. Antibiotic concentration in the elution media was determined using a calibration curve of absorbance values for known concentrations of gentamicin dissolved in PBS.

#### *2.5.7 Bacterial inhibition*

The minimum inhibitory concentration (MIC) of gentamicin sulphate against *Staphylococcus aureus* (NCTC 8532) and *Staphylococcus epidermidis* (NCTC 11047) was determined using a standard broth MIC assay [31].

In addition, antibacterial efficacy of injected cement cylinders (with and without gentamicin) and implant models filled with gentamicin loaded cement was determined using an agar diffusion assay. Briefly, overnight broth cultures of *S. aureus* and *S. epidermidis* were diluted to an optical density of 0.06 (at 600 nm) and these dilutions were then used to inoculate the surface of nutrient agar plates. Holes of the approximate diameter of the cement cylinders or the implants were bored into the agar. Three samples were placed in each agar plate and incubated at 37 °C overnight to allow semi confluent lawns of growth. After this time the diameter of any inhibition zones were measured and images taken.

## 2.6 Statistics

Results are presented as mean values  $\pm$  standard deviation. Two tail, two sample t-tests were conducted in Microsoft Excel to determine any statistical significance between measured properties of different cement formulations. P values  $< 0.05$  were deemed significant. A single factor analysis of variance (ANOVA) test was conducted on inhibition zone diameter measurements between the three groups of different pore channel orientations (Fig. 7).

## 3.0 Results

### 3.1 Characterisation of calcium phosphate cements

XRD patterns of cast, injected, and injected gentamicin loaded cements were primarily matched to ICDD standards for brushite (PDF 00-009-0077) (Fig. 2a). An isolated peak at  $27.77^\circ$  was also detected in all samples, which was associated to residual  $\beta$ -TCP (PDF 00-009-0169). This peak was notably more intense in the antibiotic loaded cement compared with both blank formulations. Micrographs of cement fracture surfaces revealed two distinct particle morphologies; larger heterogeneous and finer plate-like crystals were observed in blank and gentamicin loaded injected cements (Fig. 2b). These observations are consistent with XRD data that identified two phases; the larger heterogeneous particles were consistent with micrographs of precursor  $\beta$ -TCP powder (data not shown) and brushite is known to exhibit a plate-like morphology.

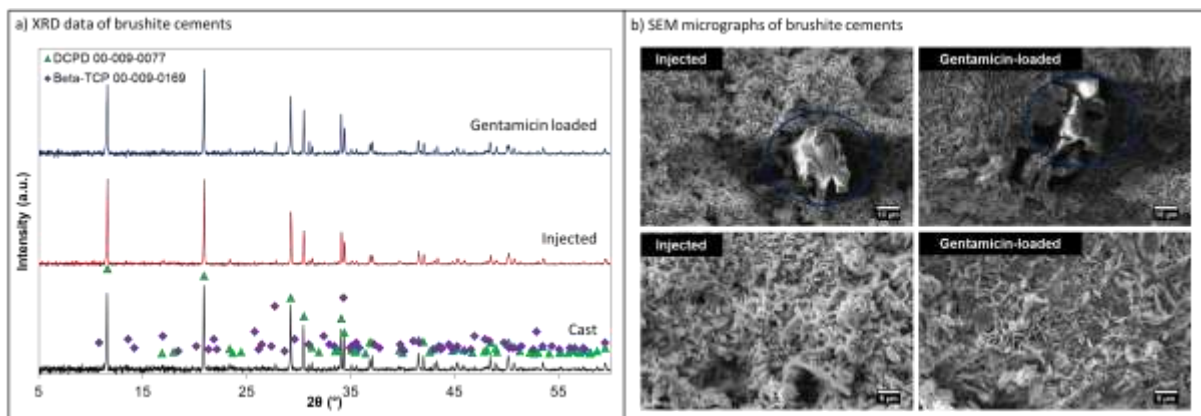


Figure 2: Characterisation of brushite cement samples a) XRD data of cast, injected, and gentamicin loaded cements illustrating matching to DCPD (▲ 00-009-0077) and  $\beta$ -TCP (◆ 00-009-0169) reference patterns, and b) micrographs illustrating residual  $\beta$ -TCP particles (blue circles) in formulated cements fragments (i without gentamicin and ii with gentamicin) and typical morphology of plate-like brushite crystals (iii without gentamicin and iv with gentamicin).

No significant variation in compressive strength ( $p = 0.92$ ) or true density ( $p = 0.14$ ) was observed between cast and injected cement cylinders (Table 1). The addition of

gentamicin was shown to significantly increase the maximum compressive strength compared with injected ( $p = 0.01$ ) samples. Addition of the antibiotic was, however, not found to significantly alter the true density ( $p = 0.35$ ) or relative porosity ( $p = 0.72$ ) compared to injected samples without gentamicin.

Table 1: Comparison of mechanical testing and helium pycnometer results for brushite cement formulations. Results presented as mean  $\pm$  standard deviation

Cement Formulation	Cast	Injected	Injected with gentamicin
Compressive Strength (MPa)	4.50 $\pm$ 0.59	4.54 $\pm$ 1.00	5.77 $\pm$ 0.69
Young's Modulus (GPa)	0.26 $\pm$ 0.13	0.17 $\pm$ 0.06	0.23 $\pm$ 0.05
Apparent Density (g/cm <sup>3</sup> )	1.58 $\pm$ 0.01	1.66 $\pm$ 0.02	1.59 $\pm$ 0.10
True Density (g/cm <sup>3</sup> )	2.13 $\pm$ 0.03	2.33 $\pm$ 0.16	2.17 $\pm$ 0.22
Relative Porosity (%)	25.59 $\pm$ 1.24	28.77 $\pm$ 5.03	26.38 $\pm$ 9.44

Micro-CT data was consistent with XRD analysis since it revealed the presence of two phases, distinguished by different grey scale values, within all cement cylinders (Fig. 3). The pixels associated with higher grey scale values (i.e. whiter) may be associated with  $\beta$ -TCP particles since it is a higher density than brushite. Unreacted  $\beta$ -TCP particles were heterogeneously dispersed throughout all samples as demonstrated in grey scale images (Fig. 3). It is important to note that a good agreement was observed between grey scale and binary micro-CT data; this demonstrates that appropriate thresholding techniques were used prior to 3D analysis.

3D analysis was used to calculate the porosity (open and closed) and  $\beta$ -TCP content of cement formulations (Fig. 3). The porosity within all samples was predominantly open (> 90% of the total porosity), i.e. connected to the extremity of the cement cylinder. Closed pores within samples were generally distributed at the extremities of the cement cylinders (Fig. 3) and > 85% were < 24.4  $\mu$ m (Table 2). Manufacturing via injection was found to increase the cement porosity and  $\beta$ -TCP content compared with casting (Fig. 3). Addition of gentamicin was shown to increase  $\beta$ -TCP content compared with unloaded injected cylinders. Notably a higher volume of open and closed pores within cast cements (35, 16%) were > 24.4  $\mu$ m compared with injected without (16, 6%) and with gentamicin (8, 0.5%) samples (Table 2).

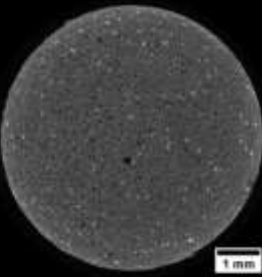
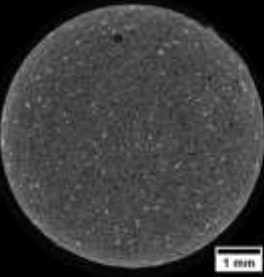
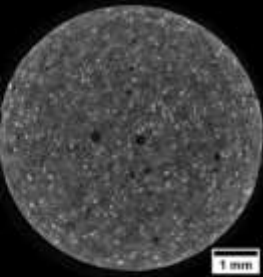
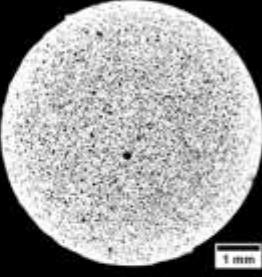
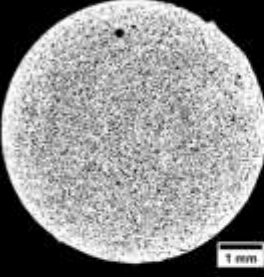
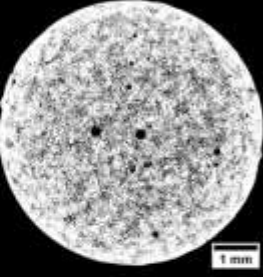
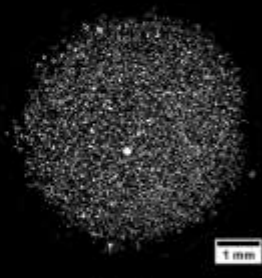
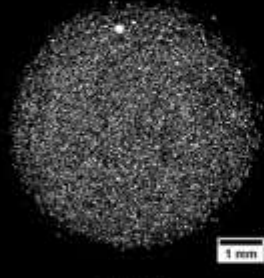
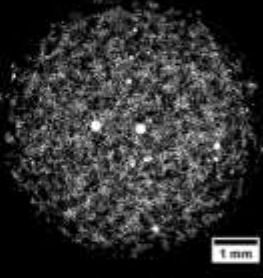
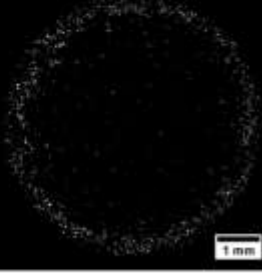
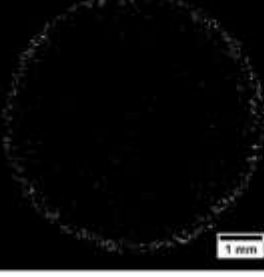
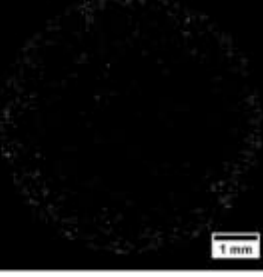
	Cast	Injected	Injected with gentamicin
Grey scale cement			
Binary cement			
Binary open porosity			
Binary closed porosity			
Total Porosity	17.9%	25.4%	23.2%
Open Porosity	16.5%	24.5%	22.6%
Closed Porosity	1.4%	0.7%	0.6%
$\beta$ -TCP Content*	3.0%	6.3%	8.9%

Figure 3: Images illustrating the 2D solid and pore structure of cement cylinders, notably the presence of two distinguishable phases can be observed in grey scale cement micrographs.

\*Calculated as a % of the total solid volume.

Table 2: Pore size range of open and closed porosity within cement formulations calculated from micro-CT data

Pore Size Range ( $\mu\text{m}$ )	Volume Within Range (%)					
	Open Porosity			Closed Porosity		
	Cast	Injected	Injected with gentamicin	Cast	Injected	Injected with gentamicin
4.9 - <14.6	16.7	31.2	38.8	39.0	59.6	87.8
14.6 - <24.4	48.3	52.9	53.5	46.9	34.7	11.7
24.4 - <34.1	23.9	12.5	5.87	11.1	5.07	0.41
34.1 - <43.8	8.15	2.52	0.77	2.68	0.60	0.08
43.8 - <53.6	1.56	0.35	0.30	0.35	0	0
53.6 - <63.3	0.29	0.08	0.21	0.04	0	0
63.3 - < 200	1.14	0.47	0.55	0	0	0

Micro-CT was used to reveal the morphology, size, and surface topography of SLM parts before being filled with cement (Fig. 4). All orientations of hole designs were found to penetrate into the reservoir region (Fig. 4a) and the internal hole geometry was found to exhibit a similar degree of surface roughness to the extremities of the parts (Fig. 4b). Average measurements of hole size (Fig. 4c) revealed that the vertical orientation adhered most closely to the CAD design of 1000  $\mu\text{m}$ . Interestingly, the standard deviation of 45° inclined hole measurements was notably greater than other orientations. Statistical analysis revealed no significant differences between any two pairs of horizontal holes. Vertical holes 2 and 4 were shown to be significantly different ( $p = 0.02$ ). A number of pairs of individual inclined holes exhibited significantly different sizes and holes 2 and 3 were shown to be highly significantly different ( $p = 0.00$ ). Overall, the size distribution of the horizontal hole measurements were shown to be vastly different from both the vertical and inclined channels ( $p < 0.001$ ).

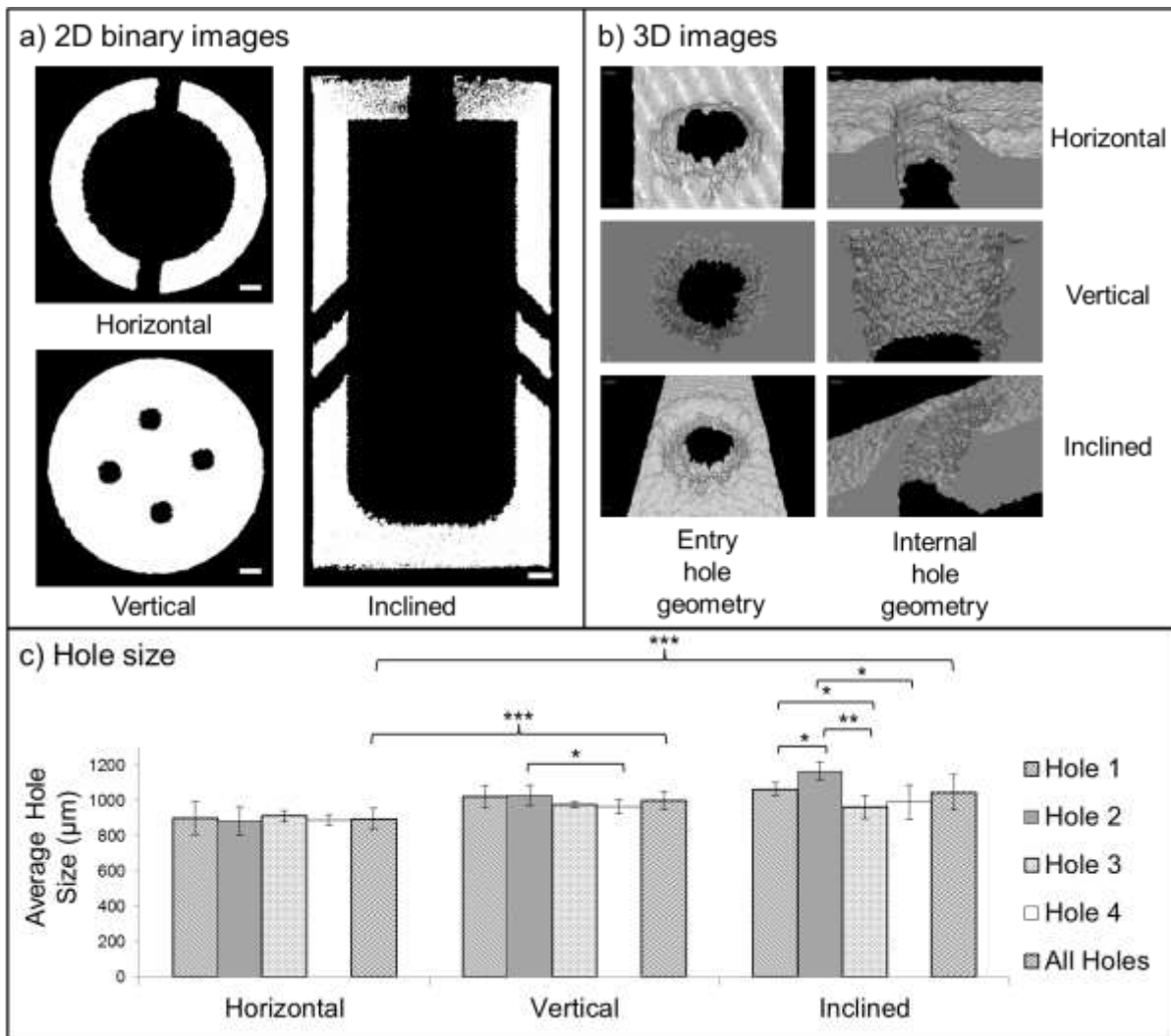


Figure 4: Microstructure of SLM implants a) 2D binary images of hole geometries (scale bars 1 mm), b) 3D reconstruction of hole ROI, and c) measurements of hole size presented as mean  $\pm$  standard deviation ( $n=4$  for individual hole measurements and  $n=16$  for all hole measurements). \* $p<0.05$ , \*\* $p<0.01$ , \*\*\* $p<0.001$

Visualisation of the internal structure of SLM parts filled with gentamicin cement was achieved using micro-CT (Fig. 5). Coronal and axial slices through the middle of the implants revealed defects in the cement within all of the models, in particular for vertical pore geometries. Using CTvox software, greyscale values corresponding to the cement were segmented (Fig. 6 – 3D rendered cement volumes). Overall this demonstrated that the implants were filled with cement in the reservoir and the pore channels of all orientations.

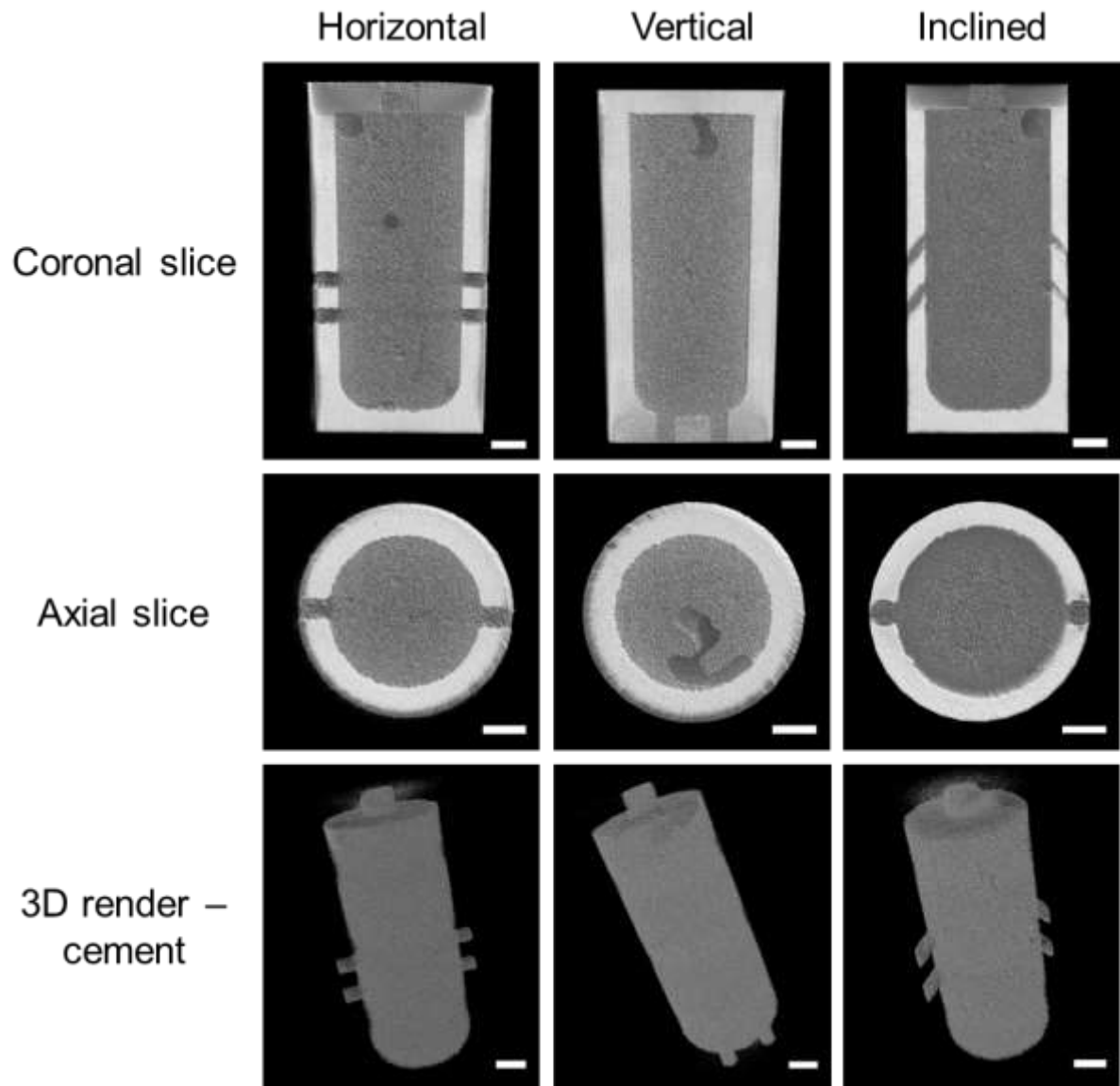


Figure 5: 3D visualisation of gentamicin loaded cement within demonstration implants (scale bars 2 mm)

As expected, the cumulative release of gentamicin from bare cement cylinders ( $\approx 37\%$ ) was shown to be substantially greater than any of the SLM implants filled with antibiotic loaded cement (Fig. 6). Interestingly, despite each of the SLM part CAD models exhibiting the same surface pore area (four holes of 1 mm diameter), after 6 h the total quantity of gentamicin released from implants with different channel orientations was notably different; vertical 28%, horizontal 10%, and inclined 5%.

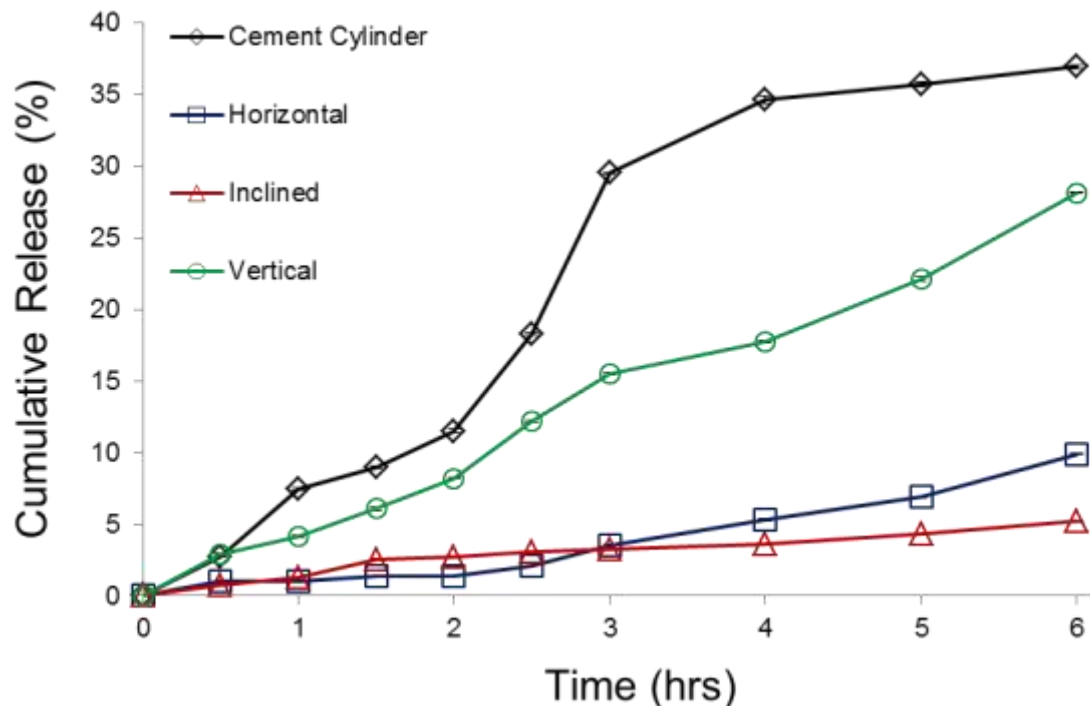


Figure 6: Cumulative release of gentamicin from brushite cement cylinders and cement filled implants. Result represented as mean  $\pm$  standard deviation ( $n=3$ )

The MIC of gentamicin against *S. aureus* and *S. epidermis* was found to be 16 and 1  $\mu\text{g/mL}$ , respectively. To confirm whether the concentrations of gentamicin released from samples (Fig. 6) were sufficient to inhibit the growth of *S. aureus* and *S. epidermis* an agar diffusion study was conducted ( Fig. 7). Near circular inhibition zones were observed for blank and gentamicin cement samples against *S. aureus*, and only for gentamicin loaded cement against *S. epidermis* ( Fig. 7b). Without gentamicin the cements did not inhibit the growth of *S. epidermis*.

SLM parts were all shown to elute sufficient concentrations of gentamicin to inhibit the growth of both bacterial cultures (Fig. 7c). For all SLM designs irregularly shaped inhibition zones were observed. To reflect the irregular shape of the inhibition zones, the minimum and maximum diameters were approximated for each sample and the average calculated for each plate ( $n = 3$ , Fig. 7d and e). In some cases, samples with horizontal and inclined channels exhibited the maximum diameter of inhibition



adjacent to where the channels were located. This led to more irregularly shaped inhibition zones; however, two-way paired t-tests conducted between minimum and maximum diameter measures only revealed statistical significance for implants with horizontally orientated pore channels ( $p = 0.05$  *S. aureus*,  $p = 0.004$  *S. epidermis*). Single factor ANOVA tests did not show any significance between the mean diameters for the three implant orientations for either bacterial species. Notably, areas of no growth for inclined and vertical SLM parts cultured with *S. aureus* and horizontal samples with *S. epidermis* were found to overlap; this made it difficult to determine the diameter of the zone contributed by individual samples.

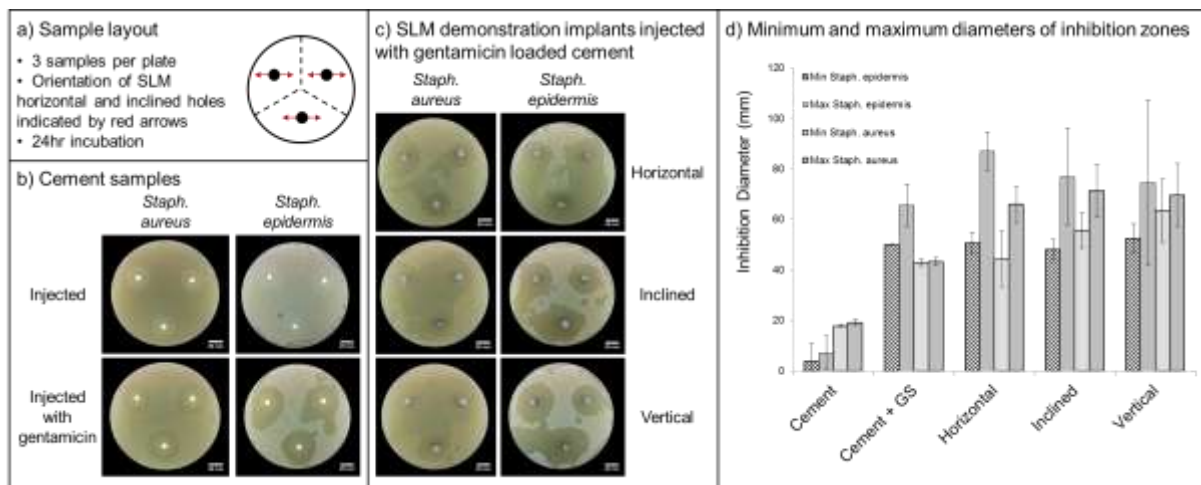


Figure 7: Agar plates after overnight culture of *staph. aureus* and *staph. epidermis* demonstrating a) sample layout; clear zones of bacterial inhibition on b) cement cylinders c) SLM parts; and d) minimum and maximum diameters of bacterial inhibition zones. Results presented as mean  $\pm$  standard deviation ( $n=3$ )

#### 4. Discussion

Set cements consist of three phases; product phase (brushite), residual reactant phase ( $\beta$ -TCP), and porosity. While both reactant and residual components contribute to stress resistance, porosity provides no support to the structure and so limits strength [32]. It is also important to note the inverse relationship between the largest pore size and critical tensile strength, as noted by Griffith [33]. A number of other factors are known to influence cement strength, including the degree of residual product, which may act as an aggregate and positively impact stress resistance if it is of a higher density [34] and [35]. Compared with cast samples, the average compressive strength was shown to improve as a result of injection and addition of gentamicin to the liquid phase, i.e.  $\sigma_{\text{cast}} \approx \sigma_{\text{injected}} < \sigma_{\text{injected}}^{\text{gentamicin}}$  (Table 1). This trend correlates with an increase in aggregate phase quantity, i.e. residual  $\beta$ -TCP content (Fig. 3). Since the microstructure of cast and injected samples without gentamicin was not obviously different it may be assumed

that the positive influence of residual  $\beta$ -TCP dominates the effect of porosity changes for these samples. Interestingly, Bohner et al. noted an improvement in tensile strength of brushite cements as a result of gentamicin addition [36]. This was ascribed to the decrease in size and thickness of DCPD particles due to the presence of sulphate ions in gentamicin ( $35 \pm 2\%$ ). A similar morphological change was observed between injected samples with and without gentamicin (Fig. 2b). Therefore the strength improvement as a result of gentamicin incorporation may be attributed to a compounding effect of a greater amount of residual  $\beta$ -TCP and a finer microstructure. For this study, compressive strength was determined at one time point. The trends observed may be expected to vary as a result of different profiles of antibiotic elution and material dissolution. It may be interesting to explore the time dependent relationships of mechanical properties in future work. However, if the cement is housed within a metallic component its strength would contribute negligibly to the total and therefore would not require optimisation.

The average values of porosity measured using helium pycnometer (Table 1) and micro-CT (Fig. 4) for injected cement samples were within one standard deviation of each other. For cast samples, however, the porosity value calculated from micro-CT analysis (17.9%) was significantly outside the average calculated from helium pycnometer measurements ( $25.6 \pm 1.2\%$ ). The detection levels achievable via micro-CT (1–2  $\mu\text{m}$ ) are far larger than those for helium pycnometer (2–50 nm). There are three types of porosity presence in set cements; gel (intrinsic to the structure), capillary (formed via evaporation of excess water), and macroporosity. Since the typical sizes of both gel (0.5–10 nm) and capillary (5 nm–5  $\mu\text{m}$ ) pores fall largely outside the limit of micro-CT, differences in porosity values obtained using these two modalities are only to be expected. The use of micro-CT enabled open and closed porosity to be distinguished, visualised, and quantified (Fig. 3 and Table 2). This revealed that gentamicin loaded cements exhibited a smaller volume fraction of open and closed pores  $> 24.4 \mu\text{m}$  compared with other samples. The compressive strength of brittle materials will be related closely to the size of the defect encountered in the maximum stress field from which the fracture originates. A clear reduction in the frequency of larger defects was shown in gentamicin loaded samples (Table 2), which suggests why this formulation exhibited a significantly higher compressive strength (Table 1).

Micro-CT was used to probe the internal structure of SLM parts and revealed minor defects within all of the structures (Fig. 4a). In particular, the degree of porosity seen in binary coronal slices of inclined parts can be seen to be greater in the uppermost layers. During SLM the depth of laser penetration may be greater than the thickness of one layer. As such the layers built first may be consolidated to a greater extent as they are passed over by the laser more times than those layers at the top of the

build. The observed honey-comb like microstructure (Fig. 4a – inclined part near to 2 mm diameter hole) and the rough internal surface topography of the holes (Fig. 4b) are commonly observed with partial powder melting, which occurs if the energy input is insufficient to induce significant melting of the powder particles. Song et al. demonstrated that laser power and scanning speed strongly effect the processing mechanism (melting with cracks, continuous melting, and partial melting), which in turn affects surface topology, part density, and micro-hardness [37]. The inherent micro-roughness of SLM parts may be advantageous to cell adhesion and differentiation [38], however, this surface topography is known to limit fatigue performance [26]. Optimisation of manufacturing and post-processing parameters (e.g. polishing) will be critical to manufacturing implants that have sufficient mechanical properties and exhibit surfaces that facilitate cellular adhesion but limit bacterial adhesion. In future studies, particularly those concerning long-term implants, it will be important to assess whether the addition of pore channels to the structure facilitates biofilm development.

Computed tomographic 3D rendering of implant models filled with gentamicin-loaded cements revealed macroscopic porosity within all designs (Fig. 5 coronal slice). The majority of these defects were observed at the top of the designs where the internal architecture of the manufactured part forms a right angle. In casting, this type of defect is often called back-pressure porosity and is caused by inability of the air in the mould to escape or by the pressure gradient that displaces air pockets towards the end of the mould [39]. It is therefore suggested that future designs should have curved internal surfaces to minimise back-pressure porosity formation. Furthermore, it appears that a greater volume of air remains in the structure when the pores are orientated parallel to the direction of injection, i.e. vertical, since this was the only sample where defects were visualised in the axial slice (Fig. 5). This orientation of pores is likely to have a lower backpressure compared with pores located on the side of the implant as such it appears less entrapped air is forced out of the reservoir. Baroud et al. concluded that high cement viscosity is required to stabilise cement flow in vertebroplasty; however, this was shown to negatively impact the injectability and working time of the formulation [40]. In future work it may be interesting to assess any trade-off between increasing the viscosity of the cement system, for example by increasing the powder to liquid ratio, and the ability of the cement to fully fill the implant. Alternatively, vibration could be used to expel air bubbles from the implant, although this would only be viable if the cavity were filled before implantation. The surface finish of the internal reservoir may also be expected to influence the flow of the injected material. Inherently, SLM parts exhibit a rough surface topography, as demonstrated in micro-CT images (Fig. 4 and Fig. 5), therefore it is suggested that optimisation of surface finishing methods, such as tumbling and polishing, may also be required.

Diffusion occurs as a result of a concentration gradient, which is a difference in the concentration of diffusion species between two separated positions. For elution of the antibiotic to occur, the solvent (PBS), would have to infiltrate the cement porosity. The entirety of the cement cylinder surface area (approximately 680 mm<sup>2</sup>) was exposed to the surrounding media and in comparison the pore channels and injection hole total an estimated 25mm<sup>2</sup>. Therefore, the greater percentage of the gentamicin released from cement cylinders ( $\approx 37\%$ ) compared to the implant models ( $< 28\%$ ) is to be expected since the larger available surface area of the cylinder allows for faster infiltration of the cement porosity with PBS (Fig. 6). Interestingly, the release profile of gentamicin from the implant with vertically-orientated pore channels was obviously different to the horizontal and inclined samples. Since all four pore channels in the vertical design are located on one face of the model (Fig. 1), i.e. they are closer together compared with the other designs, it is probable that local infiltration of the cement with PBS would occur more quickly and as a result diffusion of the antibiotic would have been initiated earlier. In comparison, the pore channels for the horizontal and inclined implant designs were located in pairs on opposite sides of the cylinder (Fig. 1). The local pore surface area available for PBS infiltration was therefore half that of the vertical design, which may have influenced the rate and degree of cement infiltration and ultimately reduced the concentration gradient. This local change in the number of pores on each face may explain why a higher concentration of gentamicin from the vertical pores (21 mg, 28% of the total concentration incorporated in the cement) was detected within the 6 h period compared with horizontal (7.4 mg, 10%) and inclined (3.9 mg, 5%) samples. Regardless, the concentrations of gentamicin released throughout the 6 hour period exceeded the MIC for both *S. aureus* (16  $\mu\text{g/mL}$ ) and *S. epidermidis* (1  $\mu\text{g/mL}$ ), which was consistent with the results of the agar diffusion study (Fig. 7). Future work, which will involve the design of clinically specific implants, will require a longer term release study to be conducted; the time frame of this study will be matched to the desired antibiotic delivery for the chosen clinical application. Typically when an infected implant is removed antibiotics are administered intravenously for 2–8 weeks [41]. Therefore it may be necessary to extend the period in which the antibiotic is released from the implant reservoir. To achieve this, polymeric microspheres may be used to encapsulate the antibiotic, which may be incorporated into the cement [42] and [43].

Cement cylinders without gentamicin were shown to exhibit some ability to inhibit the growth of *S. aureus* but had limited effect against *S. epidermidis* ( Fig. 7b). This efficacy may be attributed to the acidity of the cement. The addition of gentamicin into the cement was clearly shown to increase the inhibitory zone for both investigated cultures. Statistical analysis demonstrated a significant difference between the minimum and maximum inhibition diameters for horizontal pore channels against both bacteria (Fig. 7d and e). Therefore this orientation may not be

preferable to ensure a symmetrical release zone. However, no significant difference was demonstrated between any measurements (i.e. minimum and maximum diameters) for each of the three orientations. Generally, this assay demonstrated the importance of considering the number and location of pores required to ensure that all cultures are eradicated. Optimisation of this inhibition in 3-dimensions will be required to translate this concept to the clinic; however introduction of further pore channels will need to be traded off against any impact on mechanical integrity.

Overall, we have demonstrated that there is further added value to be gained by full utilisation of the geometrical freedom made possible by AM. Promisingly, we have shown the ability to use such a strategy to manufacture a structure that eludes clinically-relevant concentrations of antibiotic. Interestingly, the back-pressure porosity observed within the cement cavity (Fig. 5) raises the question as to whether such an implant should be filled prior to implantation or in-situ. The former would facilitate the use of methods, such as vibration, to minimise any defects within the injected material. This option may be preferable so as not to increase operating times and to ensure greater reproducibility. Alternatively, in some instances (e.g. a screw) overfilling of the implant once it is implanted may provide some additional torsional stability. Future development of this technology will require mechanical optimisation of the implant design for the intended clinical application. Introduction of a lattice structure, such as that illustrated in Fig. 1b, within the designed cavity region may be required to match the implant mechanical properties to the surrounding tissue. This would avoid stress risers that can predispose to mechanical failure.

This work is a proof of concept demonstration of the potential of AM to allow novel geometries in orthopaedic implants. There are, however, several specific clinical applications that may benefit from an orthopaedic implant capable of providing both structural support and the potential for long-term release of a drug from a reservoir. The first is in two-stage revisions for infected arthroplasty. One problem with this process is that the mechanical properties of antibiotic-loaded PMMA spacer are not suitable for significant weight-bearing and thus patients' mobility is severely compromised during this time. If an AM implant containing an antibiotic-eluting reservoir was used instead (such as illustrated in Fig. 1b), then the patients would be better able to weight-bear in the interim period with the benefits of greater independence, reduced loss of cardiovascular and musculoskeletal condition, and reduced pain. Other significant problems with the standard methodology are that the choice and dose of antibiotic suitable for loading into PMMA spacers are limited. The ability to use a wider range or even mixture of antibiotics in the implant would allow more specificity in treatment. The ability to increase the dose available for elution could increase the duration of treatment. These advantages would be particularly useful in an era of ever-increasing antibiotic resistance. The second clinical

application of such a technology could be in orthopaedic tumour surgery. Tumour excision is often followed by implantation of prostheses to maintain mechanical function. If such prostheses could contain a reservoir of a chemotherapeutic agent to be eluted into the site of tumour excision then it may be possible to reduce the incidence of local recurrence. The ease with which AM can be used to produce bespoke prostheses would be of particular advantage in this application given that bone tumours may occur in such a wide variety of anatomical locations. Finally, manufacturing an intramedullary nail with the capability of delivering osteogenic factors or even osteoblasts to the fracture site may confer clinical benefit, either in primary surgery or as a treatment for fracture non-union.

## **5. Conclusions**

Cylindrical Ti-6Al-4V implants incorporating a surface connected reservoir region were successfully manufactured via SLM and filled with gentamicin loaded brushite cement. Implant surfaces were shown to exhibit micro-roughness, which will require further investigation to assess any trade-off between cellular attachment and bacterial adhesion as well as fatigue performance. Interestingly, pore channels built parallel to the build bed, i.e. horizontal, were shown to exhibit less size variability than vertically or inclined pore orientations. This observation will be taken into account as the concept is progressed towards clinical use.

Micro-CT revealed the presence of microscopic defects within cement injected into implants of all pore orientations. However, this was observed to be more pronounced when the flow of cement was parallel to the orientation of pore channels (i.e. vertical), which was attributed to a lower back-pressure dispelling less entrapped air. Due to the presence of back-pressure porosity within all implant designs it is suggested that it may be optimal to fill such implants prior to implantation in a controlled environment to improve reproducibility and not prolong operation times.

Incorporation of the antibiotic cement within the implant models was shown to control the release compared with a blank cement cylinder. Over 6 h the concentration of gentamicin released from all orientations of pore channel exceeded the MIC of both *S. aureus* and *S. epidermidis*. The assertion made from the release study was confirmed by demonstrating zones of bacterial inhibition using an agar diffusion assay. Interestingly, some directionality of antibiotic release was observed for the horizontal and inclined pore channel implants. Overall, this study highlights that there is still much potential to further utilise AM in healthcare technologies to add new implant functionality.

## **Acknowledgements**

The authors would like to acknowledge the Engineering and Physical Sciences Research Council (grant number EP/L020815/1) for funding this research. Prof. Uwe

Gbureck (University of Würzburg) is acknowledged for providing the  $\beta$ -TCP powder used in this study.

## References

- [1] L. Pulido, E. Ghanem, A. Joshi, J.J. Purtill, J. Parvizi, *Clin. Orthop. Relat. R* 466 (2008) 1710–1715.
- [2] N.J. Hickok, I.M. Shapiro, *Adv. Drug Deliv. Rev.* 64 (2012) 1165–1176.
- [3] J.R. Crockarell, A.D. Hanssen, D.R. Osmon, B.F. Morrey, *J. Bone Joint Surg.* 80 (1998) 1306–1313.
- [4] G. Selmon, R. Slater, J.N. Shepperd, E. Wright, *J. Arthroplast.* 13 (1998) 114–115.
- [5] B.A. Masri, K.P. Panagiotopoulos, N.V. Greidanus, D.S. Garbuz, C.P. Duncan, *J. Arthroplast.* 22 (2007) 72–78.
- [6] D. Neut, H. van de Belt, J.R. van Horn, H.C. van derMei, H.J. Busscher, *Biomaterials* 24 (2003) 1829–1831.
- [7] H.v.d. Belt, D. Neut, W. Schenk, J.R.v. Horn, H.C.v.d. Mei, H.J. Busscher, *Acta Orthop.* 72 (2001) 557–571.
- [8] W.A. Jiranek, A.D. Hanssen, A.S. Greenwald, *J. Bone Joint Surg.* 88 (2006) 2487–2500.
- [9] J.A. DiPisa, G.S. Sih, A.T. Berman, *Clin. Orthop. Relat. R* 121 (1976) 95–98.
- [10] E. Fernández, M. Ginebra, O. Bermudez, M. Boltong, F.C. Driessens, J. Planell, *J. Mater. Sci. Lett.* 14 (1995) 4–5.
- [11] M. Stańczyk, B. Van Rietbergen, *J. Biomech.* 37 (2004) 1803–1810.
- [12] G. Lewis, *J. Biomed. Mater. Res.* 38 (1997) 155–182.
- [13] T. Siebel, J. Kelm, M. Porsch, T. Regitz, W. Neumann, *Acta Orthop. Belg.* 68 (2002) 150–156.
- [14] P.-H. Hsieh, C.-H. Shih, Y.-H. Chang, M.S. Lee, H.-N. Shih, W.-E. Yang, *J. Bone Joint Surg.* 86 (2004) 1989–1997.
- [15] C.F. Wolf, N.Y. Gu, J.N. Doctor, P.A. Manner, S.S. Leopold, *J. Bone Joint Surg.* 93 (2011) 631–639.
- [16] H. Rack, J. Qazi, *Mater. Sci. Eng. C* 26 (2006) 1269–1277.
- [17] J. Giannatsis, V. Dedoussis, *Int. J. Adv. Manuf. Technol.* 40 (2009) 116–127.
- [18] S.H. Huang, P. Liu, A. Mokasdar, L. Hou, *Int. J. Adv. Manuf. Technol.* 67 (2013) 1191–1203.
- [19] S.J. Hollister, *Nat. Mater.* 4 (2005) 518–524.
- [20] C.-T. Kao, C.-C. Lin, Y.-W. Chen, C.-H. Yeh, H.-Y. Fang, M.-Y. Shie, *Mater. Sci. Eng. C* 56 (2015) 165–173.
- [21] S.C. Cox, J.A. Thornby, G.J. Gibbons, M.A. Williams, K.K. Mallick, *Mater. Sci. Eng. C* 47 (2015) 237–247.
- [22] C. Qiu, N.J. Adkins, M.M. Attallah, *Mater. Sci. Eng. A* 578 (2013) 230–239.
- [23] A. Fukuda, M. Takemoto, T. Saito, S. Fujibayashi, M. Neo, D.K. Pattanayak, T. Matsushita, K. Sasaki, N. Nishida, T. Kokubo, *Acta Biomater.* 7 (2011) 2327–2336.
- [24] L. Mullen, R.C. Stamp, W.K. Brooks, E. Jones, C.J. Sutcliffe, *J. Biomed. Mater. Res. B Appl. Biomater.* 89 (2009) 325–334.
- [25] J. Vaithilingam, S. Kilsby, R.D. Goodridge, S.D. Christie, S. Edmondson, R.J. Hague, *Mater. Sci. Eng. C* 46 (2015) 52–61.
- [26] K.S. Chan, M. Koike, R.L. Mason, T. Okabe, *Metall. Mater. Trans. A* 44 (2013) 1010–1022.
- [27] P. Jamshidi, R.H. Bridson, A.J. Wright, L.M. Grover, *Biotechnol. Bioeng.* 110 (2013) 1487–1494.
- [28] U. Gbureck, O. Grolms, J. Barralet, L. Grover, R. Thull, *Biomaterials* 24 (2003) 4123–4131.
- [29] Z. Xia, L.M. Grover, Y. Huang, I.E. Adamopoulos, U. Gbureck, J.T. Triffitt, R.M. Shelton, J.E. Barralet, *Biomaterials* 27 (2006) 4557–4565.
- [30] M. Hofmann, A. Mohammed, Y. Perrie, U. Gbureck, J. Barralet, *Acta Biomater.* 5 (2009) 43–49.
- [31] I. Wiegand, K. Hilpert, R.E. Hancock, *Nat. Protoc.* 3 (2008) 163–175.
- [32] E. Ryshkewitch, *J. Am. Ceram. Soc.* 36 (1953).
- [33] A.A. Griffith, *Philos. T. Roy. Soc. A* 163–198 (1921).
- [34] M. Bohner, F. Theiss, D. Apelt, W. Hirsiger, R. Houriet, G. Rizzoli, E. Gnos, C. Frei, J. Auer, B. Von Rechenberg, *Biomaterials* 24 (2003) 3463–3474.
- [35] S. Mindess, *Structure and Performance of Cements*, Applied Science Publishers, London and New York, 1983 319–363.



- [36] M. Bohner, J. Lemaître, P.V. Landuyt, P.Y. Zambelli, H.P. Merkle, B. Gander, *J. Pharm. Sci.* 86 (1997) 565–572.
- [37] B. Song, S. Dong, B. Zhang, H. Liao, C. Coddet, *Mater. Des.* 35 (2012) 120–125.
- [38] P.H. Warnke, T. Douglas, P. Wollny, E. Sherry, M. Steiner, S. Galonska, S.T. Becker, I.N. Springer, J. Wiltfang, S. Sivananthan, *Tissue Engineering Part C: Methods* 15 (2008) 115–124.
- [39] K.J. Anusavice, C. Shen, H.R. Rawls, *Phillips' Science of Dental Materials* Elsevier Health Sciences 2012.
- [40] G. Baroud, M. Crookshank, M. Bohner, *Spine* 31 (2006) 2562–2568.
- [41] S.J. McConoughey, R. Howlin, J.F. Granger, M.M. Manring, J.H. Calhoun, M. Shirtliff, S. Kathju, P. Stoodley, *Future Microbiol* 9 (2014) 987–1007.
- [42] W. Chaisri, A.H. Ghassemi, W.E. Hennink, S. Okonogi, *Colloids Surf. B: Biointerfaces* 84 (2011) 508–514.
- [43] J. Schnieders, U. Gbureck, R. Thull, T. Kissel, *Biomaterials* 27 (2006) 4239–4249.